Revealing the Cell-Material Interface with Nanometer Resolution by Focused Ion Beam/Scanning Electron Microscopy

Please check the document version of this publication:

• A submitted manuscript is the version of the article upon submission and before peer-review. There can be important differences between the submitted version and the official published version of record. People interested in the research are advised to contact the author for the final version of the publication, or visit the DOI to the publisher's website.
• The final author version and the galley proof are versions of the publication after peer review.
• The final published version features the final layout of the paper including the volume, issue and page numbers.

Link to publication

ACS NANO

ARTICLE

Revealing the Cell−Material Interface with Nanometer Resolution by Focused Ion Beam/ Scanning Electron Microscopy

Francesca Santoro,*,[†,¶] Wenting Zhao,[†,‡] Lydia-Marie Joubert,[§] Liting Duan,[†] Jan Schnitker,[∥] Yoeri van de Burgt,[‡,□] Hsin-Ya Lou,[†] Bofei Liu,[‡] Alberto Salleo,[‡] Lifeng Cui,[⊥] Yi Cui,[‡,#] and Bianxiao Cui*,[†]

[†]Department of Chemistry, [‡]Department of Material Science and Engineering, and [§]CSIF Beckman Center, Stanford University, Stanford, California 94305, United States

[∥]Institute of Bioelectronics ICS/PGI-8, Forschungszentrum Juelich, Juelich, 52428, Germany

[⊥]Department of Material Science and Engineering, Dongguan University of Technology, Guangdong 523808, China

[#]Stanford Institute for Materials and Energy Sciences, SLAC National Accelerator, Menlo Park, California 94025, United States

S *Supporting Information*
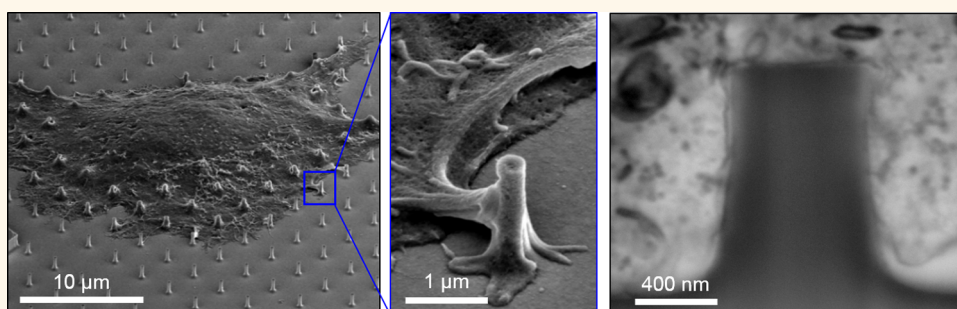
ABSTRACT: The interface between cells and nonbiological surfaces regulates cell attachment, chronic tissue responses, and ultimately the success of medical implants or biosensors. Clinical and laboratory studies show that topological features of the surface profoundly influence cellular responses; for example, titanium surfaces with nano- and microtopographical structures enhance osteoblast attachment and host−implant integration as compared to a smooth surface. To understand how cells and tissues respond to different topographical features, it is of critical importance to directly visualize the cell− material interface at the relevant nanometer length scale. Here, we present a method for *in situ* examination of the cell-to- material interface at any desired location, based on focused ion beam milling and scanning electron microscopy imaging to resolve the cell membrane-to-material interface with 10 nm resolution. By examining how cell membranes interact with topographical features such as nanoscale protrusions or invaginations, we discovered that the cell membrane readily deforms inward and wraps around protruding structures, but hardly deforms outward to contour invaginating structures. This asymmetric membrane response (inward *vs* outward deformation) causes the cleft width between the cell membrane and the nanostructure surface to vary by more than an order of magnitude. Our results suggest that surface topology is a crucial consideration for the development of medical implants or biosensors whose performances are strongly influenced by the cell-to-material interface. We anticipate that the method can be used to explore the direct interaction of cells/tissue with medical devices such as metal implants in the future.

KEYWORDS: cell−material interface, nanostructures, scanning electron microscopy, focused ion beam, ultrathin resin plasticization

Many biological applications and biomedical devices require direct contact between cells and non-biological materials.[1] In the case of medical implants, the cell-to-material interface is a key determinant for successful device integration with surrounding tissues, providing mechanical support and minimizing host foreign body responses.[2−4] Extensive clinical and laboratory studies have shown that surface topologies of nonbiological materials can significantly affect cellular and tissue responses. For example, titanium implants having a rough surface perform much better than
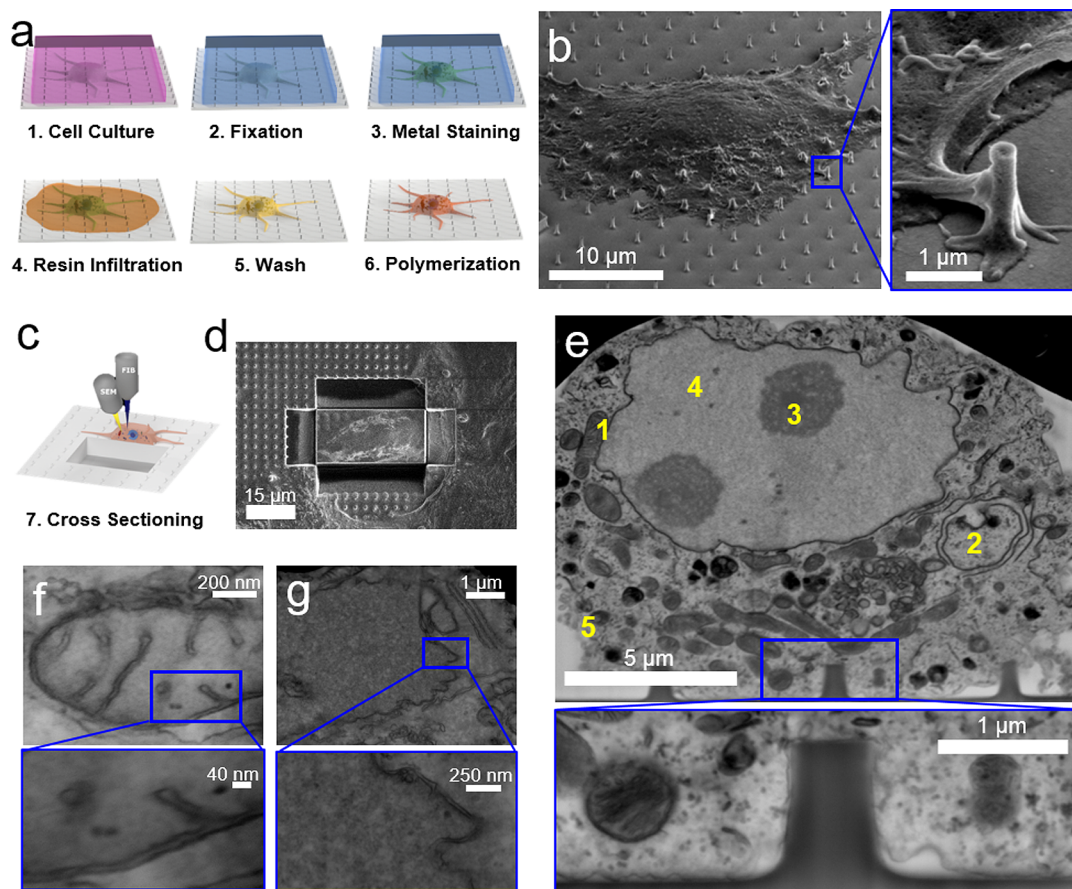
A

Figure 1. Imaging the cell-to-material interface by FIB/SEM. (a) Schematics of the sample preparation procedure by thin-layer resin plasticization with contrast enhancement. (b) SEM image of a plasticized HL-1 cell on a quartz substrate with nanopillars showing that extracellular resin is removed and the cell morphology is clearly visible. The inset shows that the membrane protrusions in contract with a nanopillar are well preserved. (c) Schematics and (d) experimental results of using FIB milling to cut trenches through the cell and the substrate and open up the interface. (e) SEM image of the interface after FIB milling revealing intracellular compartments and organelles such as mitochondria (1), intracellular membranes (2), nucleoli (3), nucleus (4), and cellular membrane (5). Inset: At the interface between the cell and the quartz substrate, the plasma membrane is shown to warp around a vertical nanopillar. Intracellular structures and local curvatures on the plasma membrane resembling clathrin-mediated endocytosis events can be identified. (f, g) Zoomed-in FIB-SEM images of mitochondria (f) and nuclear envelope (g). The insets clearly resolve the inner and outer membranes and interstitial space. Figures e−g have been acquired from backscattered detectors (voltage: 5−10 kV, current: 0.64−1.4 nA), tilt is 52°, and original images are black−white inverted.

those having a smooth surface for osteoblast attachment, host−implant integration, and the overall success of the implant.[1,5] At the cellular level, surfaces with nano- and micrometer topographical features have been shown to actively affect cell behavior such as stimulating stem cell differentiation,[6] enhancing osteoblast maturation,[7] and regulating macrophage activity.[8] In this context, understanding how cells interact with different features on the material surface is essential to study how surface topologies regulate cell signaling, guide cell migration, and control stem cell differentiation.[9−11]

The most critical feature of the cell-to-material interface is the cleft between the cell membrane and the material surface, usually in the range of 50−200 nm for flat surfaces.[12−14] Sophisticated optical techniques have been developed to measure the cleft distance, such as fluorescence interference contrast (FLIC) microscopy,[15−17] surface-generated structured illumination microscopy, and variable incidence angle FLIC microscopy (VIA-FLIC[18]). However, these interference-based techniques are limited to smooth and reflective surfaces and are not suitable for surfaces with topological features. Transmission electron microscopy (TEM) is the most widely used method to

directly visualize membrane structures at the nanoscale.[13,14,19] However, TEM requires sectioning the sample into ultrathin slices (<100 nm thickness) with mechanical knives, a procedure not compatible with a variety of substrate materials. For this reason, the support material underneath the cells has to be removed and the removal process by chemical or physical treatment is often not feasible; even if feasible, the procedure is challenging and can induce structural artifacts at the interface.[13,20]

A combination of focused ion beam (FIB) and scanning electron microscopy (SEM) constitutes an alternative approach for *in situ* imaging interfaces of any material and any desired location.[21] However, using FIB-SEM to examine the cell-to-material interface is severely limited by the lack of contrast of biological specimens and the sponge-like intracellular defects induced by hard drying procedures.[22−24] Resin-embedding preparation with heavy metals allows the visualization of intracellular structures even in the proximity of nanostructures,[25,26] but the resin matrix around the cells does not allow any visualization of the entire cell unless a 3D reconstruction of the whole specimen is performed. Recently, thin-layer resin
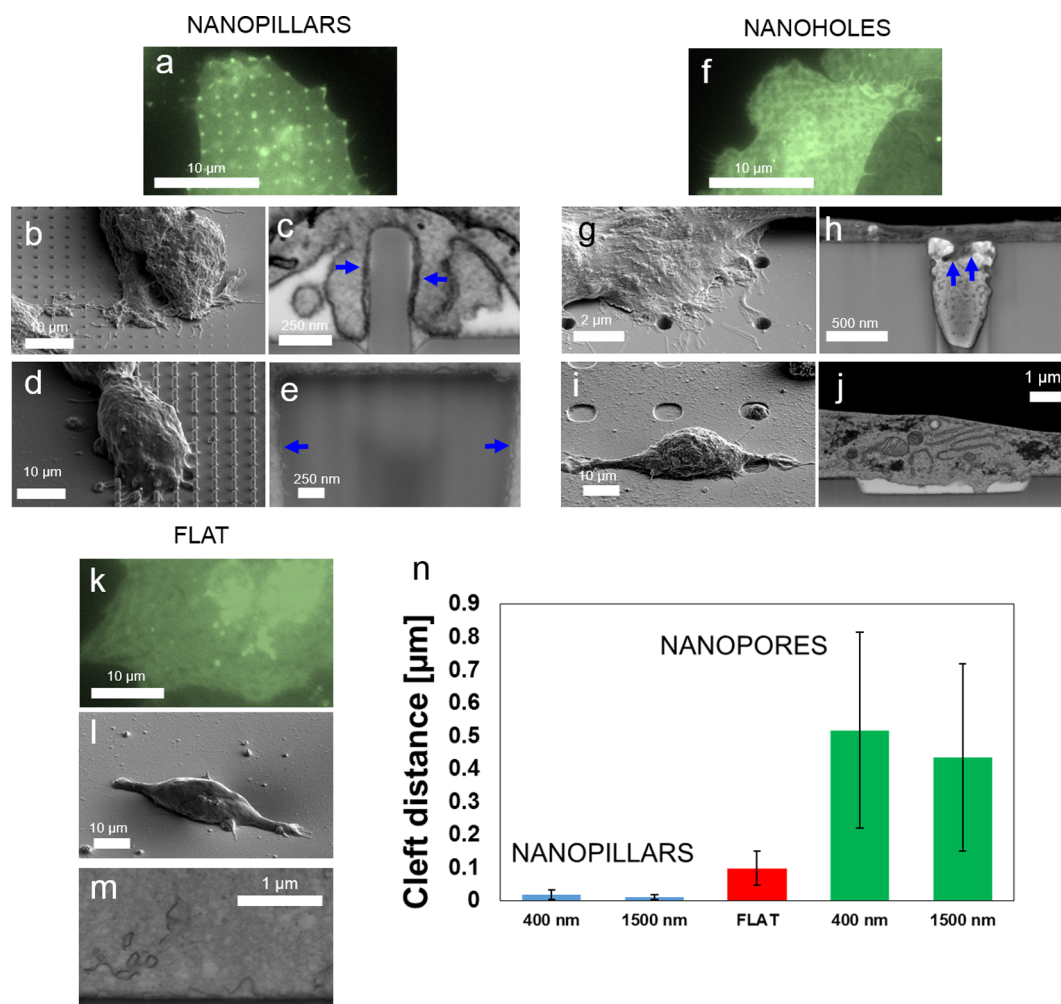
NANOPILLARS   NANOHOLES

FLAT

Figure 2. Surface topology drastically affects the cleft distance between the cell membrane and the material surface. (a, f, k) CAAX-GFP transfected cells in green on nanopillars (a), nanopores (f), and flat surface (k) showing accumulation (bright spots) of nanopillars and uniform distribution of nanopores and flat surface. (b, d, g, i, l) SEM of plasticized HEK cells on nanopillar arrays (b, d), nanopore arrays (g, i), and a flat surface (l). (c, e, h, j) FIB cross sections revealing that the plasma membrane wraps tightly around nanopillars with 400 nm (c) and 1500 nm diameter (e), while it mostly grows on top of nanopores of about 400 nm in diameter (h) and tentatively grows inside the nanopore of about 6 μm diameter but remains far away from the surface in most places (j). (m) FIB cross section of a cell on a planar silicon surface showing the membrane-to-material contact at the interface. (n) Direct measurements showing that nanopillars reduce the cleft distance as compared to flat surfaces, while nanopores drastically increase the cleft distance.

81 embedding methods have been developed to allow the
82 visualization of cells on microstructures,[24,27,28] but the contrast
83 of the resulting samples is still too low to clearly resolve the
84 membrane-to-material interface at the nanoscale. To date, there
85 is no method that can reliably resolve the plasma membrane in
86 proximity to nano- and microstructures and thus to measure
87 the cleft distance between the cell membrane and the material
88 surface. Therefore, the question of how surface topology affects
89 the cleft distance remains largely unexplored.

90   In this work, we present a FIB-SEM method that can
91 precisely resolve the cell-to-substrate interface with 10 nm
92 resolution. At the core of our FIB-SEM method is a sample
93 preparation method based on controlled thin-resin plasticiza-
94 tion of adherent cells with heavy metal staining. Unlike the
95 usual hard drying methods, this procedure embeds cells in a
96 thin plastic layer, which not only preserves the subcellular
97 structures but also provides a solid support for the subsequent
98 FIB milling.

RESULTS AND DISCUSSION

99

The thin-layer plasticization method includes five major steps: 100
cell fixation, heavy metal staining, resin infiltration, extracellular 101
resin removal, and resin polymerization (Figure 1a). Specifi- 102 f1
cally, mammalian cells cultured on the desired substrate are 103
fixed by glutaraldehyde to cross-link intracellular structures (*i.e.*, 104
proteins) so that they can withstand the subsequent staining 105
and embedding processes without altering the interstitial space 106
between the membrane and the material surface.[29,30] After 107
fixation, the cells are treated with osmium- and uranium-based 108
staining series (RO-T-O procedure[31,32] and *en bloc* staining; see 109
Experimental Procedure for details), a critical step to provide 110
high contrast to membrane and protein structures. Then, cells 111
are infiltrated with liquid epoxy-based resin. Traditional resin- 112
embedding procedures for TEM typically result in a 2−5-mm- 113
thick polymer block, preventing the visualization of the whole- 114
cell morphology. In our method, after resin infiltration and 115
before resin polymerization, a resin-removal step is introduced 116
that strips off the excess extracellular resin by first draining and, 117

C

then, flushing the sample with ethanol. This step thins down the resin coating outside the cell membrane to tens of nanometers while maintaining a stable intracellular resin embedding.[24] The final step involves curing the liquid resin to a thin layer of plastic with cells embedded inside. Since extracellular resin is largely removed, cell topography and membrane protrusions in contact with the underlying substrate are clearly visible under SEM. Figure 1b shows a resin-embedded HL-1 cell cultured on a quartz substrate with arrays of nanopillars, and Supplementary S1 shows resin-embedded PC12 cells and primary cortical neurons cultured on flat glass substrates, where fine features of the cell membrane are well preserved.

Samples prepared *via* thin-layer plasticization are directly mounted on FIB-SEM for *in situ* examination of the cell-to-substrate interface. For this purpose, we first examine a large sample area by SEM to identify locations of interest, such as places where cell membranes are in contact with topological features such as nanopillars. Once a desired area is located, it is coated with a thin layer of platinum to prevent sample damage during the next FIB milling step (see Experimental Procedure and Supplementary S2). Then, a high-energy gallium ion beam (acceleration current of 0.74 nA) is focused on the sample to cut through the platinum protection layer, the cell-embedded thin plastic layer underneath, and at least 1 μm deep into the substrate. This process is repeated to remove material and opens up a vertical surface (Figure 1c,d). Then, a low-current, *e.g.*, 80 pA, ion beam is used to remove redeposited material and polish the cross section. This step is critical for limiting the well-known curtaining phenomena and ion-induced structural damage at the interface.[33] SEM visualization of the cross section clearly shows intracellular structures as well as the interface between the cell membrane and the substrate (Figure 1e). Unlike previous FIB-SEM images that usually contain sponge-like structures with no discernible subcellular structures,[24,27,34] our FIB-SEM images show very clear subcellular structures such as the cell membrane, the nucleus, nucleoli, the nuclear envelope, mitochondria, and intracellular membranes. We note that the resin wash step of the thin-resin plasticization procedure needs to be carried out gently to avoid over-removal of the resin, which can cause cracks in the cell membrane and intracellular space. For the heavy metal staining step, either overstaining or understaining results in poor structural contrast and lower resolution, similar to TEM samples. All FIB-SEM images are black-and-white inverted. Original images are shown in Supplementary S2.

To determine the resolution of our FIB-SEM method, we have examined a group of well-characterized cellular compartments using high-magnification SEM imaging. Figure 1f shows a mitochondrion with clearly resolved inner and outer membranes (~10 nm distance) as well as the cristae structures. Figure 1g shows the structure of a nuclear envelope with well-distinguishable inner and outer membranes, which are separated by an interstitial space of about 20 nm. Endoplasmic reticulum (ER) structures as parallel running membranes can be seen in the vicinity of the nucleus, and the associated small granules attached to the membrane of the ER likely are ribosomes (Supplementary S3). Other intracellular structures such as multivesicular bodies and intracellular membrane can also be resolved in Supplementary S3. Furthermore, a high-magnification SEM image of the cell−substrate interface clearly reveals that the plasma membrane is very close to the flat substrate surface and contours around local nanopillar features (Figure 1e, inset).

The development of this FIB-SEM method allows us to quantitatively address the question of how different surface topographies affect the cell−substrate cleft distance. For this study, we engineer SiO$_2$ substrates (or Si substrates with a SiO$_2$ surface layer) with different surface geometries, including protrusions, invaginations, flat, and other complex structures (see Experimental Procedure for fabrication details). The protrusions are vertical nanopillars with diameters or lengths varying from 200 to 1500 nm, a height of 1 μm, and spacing of 3−5 μm (Figure 2b,d and Supplementary S4). The invaginations are pores with diameters varying from 200 to 6000 nm, a depth of about 500 nm to 1 μm, and a spacing of 3 μm (20 μm for the largest pore) (Figure 2g,i and Supplementary S5). A cell on a flat surface is shown in Figure 2l. The complex structures include nanotubes, nanobars, irregular nanocones, nanoletters (CUIO), and grooves, and they are shown in Supplementary S4 and S6. All substrates were coated with poly-L-lysine or fibronectin to facilitate cell adhesion. HEK or HL-1 cells were used for the studies. Cells cultured on different substrates were processed for FIB-SEM imaging using the aforementioned preparation method. SEM images of cells cultured on flat, nanopillar, and nanopore substrates before FIB milling show healthy and spread cell morphology (Supplementary S7).

The FIB-SEM imaging reveals drastic differences in how cell membranes respond to different substrate nanotopologies. For substrates with protruding structures, the cell membrane deforms readily and wraps conformally around the surface topology, as shown in Figure 2c,e and Supplementary S8, for nanopillars with 400 nm and about 1500 nm diameter, respectively. For nanopillars of all diameters the cell membrane is usually within 10−30 nm on average from the substrate surface. In sharp contrast, for substrates with invaginating structures, the cell membrane hardly deforms and does not contour the surface of nanopores or the hollow centers of the nanotubes (Supplementary S9). For small-diameter pores (Figure 2h), the cell membrane extends into the pores slightly, but the cleft distance is usually more than 10 times greater than that for nanopillars. For nanopores as large as 6 μm in diameter and 500 nm in depth, the cell membrane is still far away from the surface (Figure 2j), but some attachment points are created in the pore. For flat surfaces, the cell membrane remains close to the surface (Figure 2m). A similar phenomenon is observed in other complex structures (Supplementary S9). For protruding structures such as nanobars, CUIO nanoletters, and nanocones, the cell membrane is very close to the substrate surface, while for invaginating structures such as grooves, the cell membrane is far away from the substrate surface (Supplementary S9). For nanotubes, the cell membrane wraps tightly around the outside wall of the tube (protruding structure), while it remains far away from the inner wall of the hollow center (invaginating structure, Supplementary S9). This is a surprising result, as previous studies suggest that the cell membrane is highly deformable and can extend into pits as small as 50 nm.[35,36]

In order to evaluate the cleft formed between the plasma membrane and different surface topographies, we systematically measured the average cleft distance for surfaces with nanopillars and nanopores with comparable dimensions and flat surfaces (measurement statistics shown in Supplementary S10). As seen in Figure 2n, the cleft distance is ~100 nm (stdv 50 nm) for the

243 flat surface, which agrees with previous studies.[12,14] The cleft
244 distance decreases to ~15 nm (stdv 10 nm) for nanopillars,
245 while it increases to >400 nm for nanopores (stdv 300 nm).
246 These dramatic changes in the cleft width suggest that the
247 plasma membrane interacts with protruding and invaginating
248 surface topologies in fundamentally different ways. In addition,
249 we calculated the cleft area between the membrane and the
250 nanostructures for all the investigated nanoholes and nanopillar
251 types. The cleft index measurement confirms that the cleft area
252 increases in the presence of nanopores and decreases in the
253 presence of nanopillars (see Supplementary S10 and S11 for
254 details).

255   To corroborate the FIB-SEM studies, we also examined how
256 the plasma membrane interacts with different surface topologies
257 by fluorescence imaging. At the same time, we simultaneously
258 probed the distribution of actin filaments, which are well known
259 to participate in the dynamics and the formation of protrusions
260 or invaginations on the cell membrane.[37,38] Cells were
261 cotransfected with two plasmids, CAAX-GFP, which serves as
262 a marker for the plasma membrane, and LifeAct-RFP, which is
263 widely used to visualize F-actin in cells. Fluorescence imaging of
264 CAAX-GFP confirms that the cell membrane wraps around
265 nanopillars (bright spots due to projection of the vertical
266 membrane in Figure 2a) but not nanopores or flat surfaces
267 (Figure 2f,k). LifeAct-RFP imaging shows that F-actin
268 accumulates strongly on nanopillar locations, but is absent at
269 nanopores (Supplementary S12) and flat surfaces (data not
270 shown). This preliminary result suggests that actin filaments
271 might be involved in forming the close contact between the cell
272 membrane and the nanopillars.

273   Next, we examine whether the topological effect for the
274 interface cleft depends on the chemical composition of the
275 material. Considering that our FIB-SEM method is applicable
276 to materials with diverse composition and stiffness, we
277 compared flat and nanopillar surfaces made of quartz (Young's
278 modulus ~80 GPa) and conductive polymer blend poly(3,4-
279 ethylenedioxythiophene):polystyrenesulfonate (PEDOT,
280 Young's modulus ~1 GPa). Unlike quartz (shown as the gray
281 bottom layer in Figure 2f−i), PEDOT is conductive and
282 scatters electrons strongly (shown as the black bottom layer in
283 Figure 3b), which reduces the effective contrast of the
284 biological sample. Despite this, the FIB-SEM image in Figure
285 3b (cells before cut shown in Figure 3a) still clearly resolves the
286 cell membrane−surface gap, achieving the first cross section
287 visualization of cells on the PEDOT surface. Here, we
288 measured the effective distance of the plasma membrane
289 from the surface. The cell membrane is seen in close contact
290 with the flat PEDOT surface, and the average cleft distance is
291 measured to be 89 ± 73 nm (stdv), similar to the cleft distance
292 for the flat quartz surface at 98 ± 52 nm (stdv). Next, we
293 compared the cleft distances for nanopillar substrates made of
294 quartz and covered with a thin layer of PEDOT (Figure 3c,d).
295 Our measurements show that the average cleft distances for
296 quartz nanopillars and PEDOT nanopillars are similar (15 ±
297 2.7 nm and 11 ± 4.1 nm, stdv) but much smaller than that for
298 the flat surfaces. The statistical details of these measurement are
299 shown in Supplementary S10.

300   Finally, we explored the capabilities of the FIB/SEM method
301 for volumetric imaging and multiangle imaging. FIB-SEM
302 allows repetitive milling and imaging, allowing the investigation
303 of a volume of interest (Figure 4a). We used low current (e.g.,
304 80 pA) for sequential FIB milling, which achieves a slice
305 thickness of about 20−40 nm and well beyond the capability of
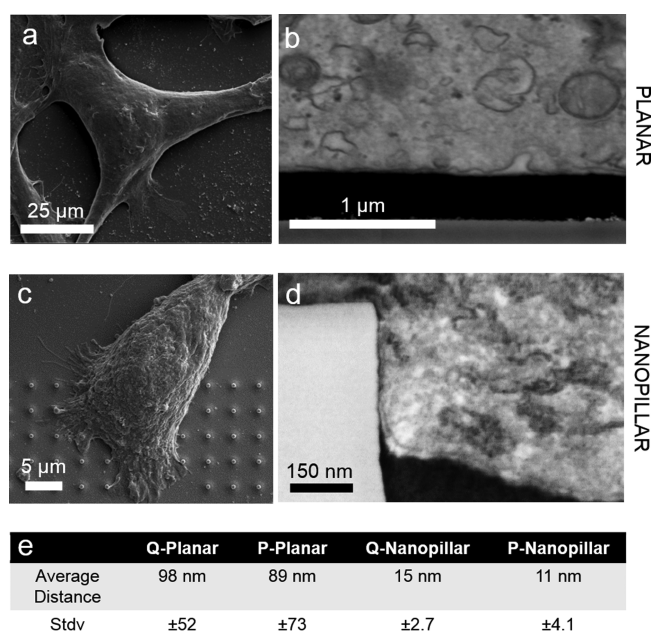

Figure 3. Comparison of quartz and PEDOT surfaces shows that the cleft distance is mainly determined by surface topologies. (a) SEM image of a plasticized HL-1 cell on planar PEDOT. (b) FIB cross section revealing the plasma membrane and local ruffling on the planar PEDOT surface. (c) SEM image of a plasticized HL-1 cell on quartz nanopillars covered with a thin layer (10−20 nm) of PEDOT. (d) FIB cross section revealing the close contact of the plasma membrane to the PEDOT superficial layer on the nanopillar. (e) Quantitative analysis of the average cleft values and the corresponding standard deviation calculated for quartz (Q) and PEDOT (P) substrates with planar and nanopillar surfaces showing that cleft values are comparable for the same structures but different materials.

e	Q-Planar	P-Planar	Q-Nanopillar	P-Nanopillar
Average Distance	98 nm	89 nm	15 nm	11 nm
Stdv	±52	±73	±2.7	±4.1

306 mechanical slicing by means of ultramicrotomes (70−200 nm).
307 Figure 4b,c show two representative cross sections of the same
308 cell (shown in Figure 4a) interacting with two different lines of
309 nanopillars. By sequentially imaging a set of 72 sequential
310 sections, we reconstructed a 3D intracellular space and its
311 interaction with nanopillars using a segmented 3D reconstruc-
312 tion method (Figure 4d, Supplementary Movie 1). In particular,
313 we modeled the 3D morphology of the nuclear envelope,
314 nucleoli, and the nonadherent cellular membrane domain,
315 which were individually constructed and overlaid on the
316 remaining structures, as shown in Figure 4e. The nuclear
317 envelope appears to be bent upward on top of a nanopillar by
318 as much as 800 nm (Figure 4f), agreeing well with our previous
319 observation by TEM.[39]

320   Unlike the ultramicrotome sectioning method, which slices
321 materials sequentially in only one direction, the FIB-SEM
322 method is highly versatile and allows sectioning of the same
323 sample with different directions at multiple locations. This
324 capability is often important for cells with protrusions such as
325 neurons. Primary cortical neurons from embryonic rats were
326 cultured on a quartz substrate with arrays of solid nanopillars.
327 After 5 days of culturing in vitro, neurons were fixed and
328 processed for FIB-SEM imaging as described earlier. The SEM
329 image in Figure 4g (inset) shows a neuron cell body together
330 with multiple neurites growing out from the cell body. We first
331 identified four regions of interest from the SEM image: the cell
332 body, neurite-1, neurite-2, and neurite-3. Then, after coating a
333 layer of Pt, FIB milling was used to cut open the interfaces
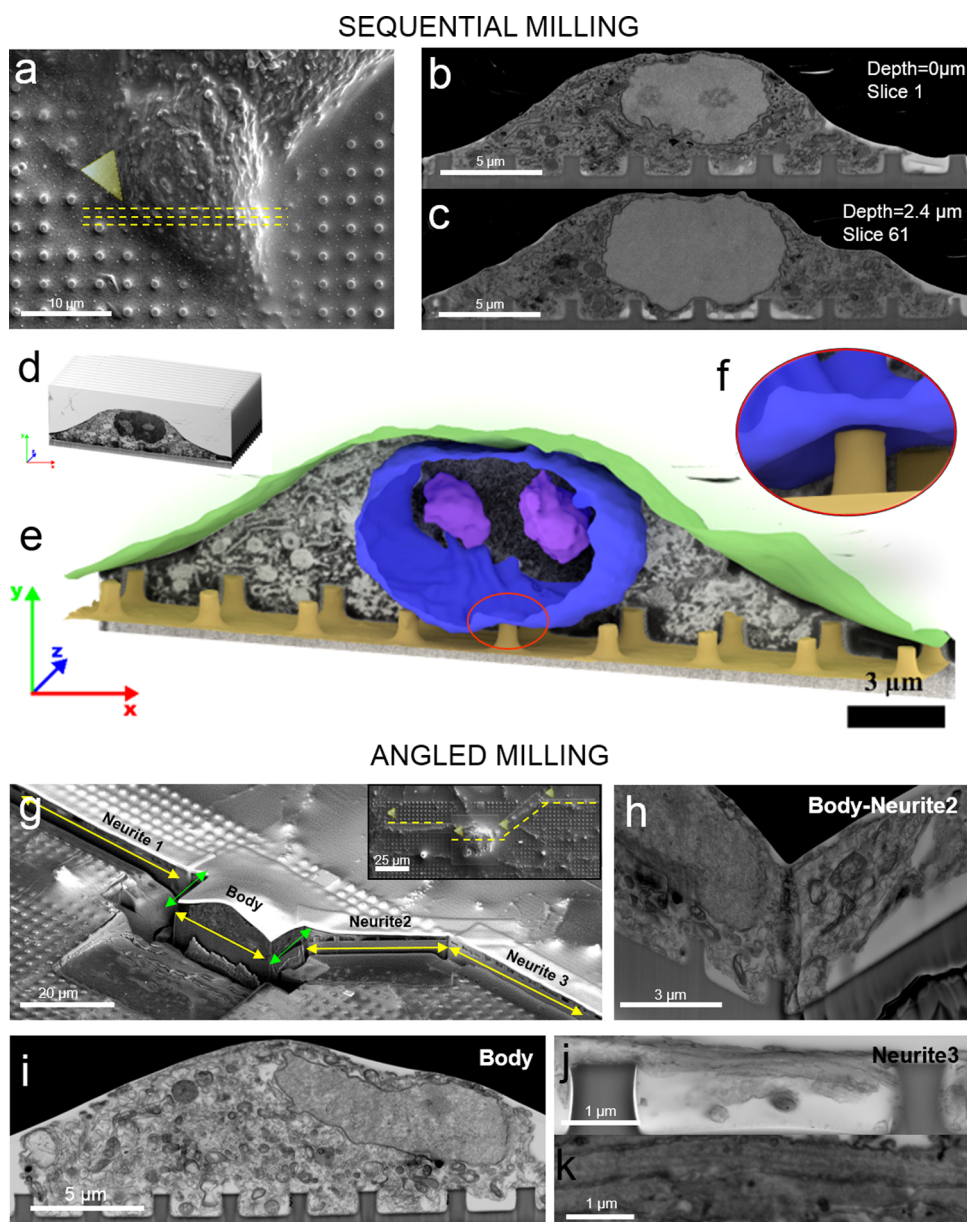
SEQUENTIAL MILLING

ANGLED MILLING

Figure 4. FIB-SEM for sequential volumetric imaging and multiangled imaging. (a) SEM image of a plasticized HL-1 on nanopillars where yellow dashed lines indicate the region of interest for the sequential milling. (b, c) SEM images of two exemplary slices from a stack of 78 slices at two different pillars' lines. (d−f) Images collected in the stack were assembled, segmented, and analyzed. Automated 3D reconstruction of the top membrane and the nuclear envelope overlaid on the SEM background image. Reconstruction shows that the nuclear envelope is deformed upward by a nanopillar. (g) FIB milling of a neuron where yellow arrows indicate the regions of interest and green lines indicate the connecting regions (the inset shows a SEM image of the same neuron before FIB milling). (h) FIB-SEM image of the body−neurite 2 connecting region opened at a 90-degree angle. (i) FIB-SEM image of the neuronal body on a line of nanopillars. (j) FIB-SEM image of neurite 3 on top of nanopillars. (k) Zoomed-in image of neurites revealing multiple longitudinally oriented microtubules parallel to the direction of the neurite.

along six connecting lines (yellow arrowed lines corresponding to four regions of interest and green arrowed lines being the connecting lines in Figure 4g). FIB-SEM imaging of the cell body shows the nucleus, a large number of intracellular organelles, and the plasma membrane wrapping around the nanopillars (Figure 4i). By multiangle milling, FIB-SEM also offers the advantage of examining a location from multiple directions, as shown by the 90-degree intersection between neurite-2 and the cell body (Figure 4h). The cross section of neurite-3 is shown in Figure 4j, which illustrates a neurite attached to the top and the side of two nanopillars. A magnified image of a neurite reveals multiple longitudinally orientated microtubules parallel to the direction of the neurite (Figure 4k), comparable in morphology to those investigated by TEM.[40,41]

CONCLUSIONS

We demonstrate a FIB-SEM method for imaging the cell-to-material interface *in situ*, without removing the substrate. The FIB-SEM method has the advantages of examining a large sample area, opening up cross sections at any desired location, achieving volume reconstruction, and performing multidirectional milling. This method achieves a high contrast and

resolution at 10 nm and is suitable to investigate the interface between the cell membrane and nonbiological materials. Our study reveals a surprising discovery that the cleft width between the cell membrane and the substrate surface is strongly influenced by the surface topology. As the cell attachment and the membrane-to-material interface strongly influence the performance of medical implants and biosensors, our study suggests that surface topology is a crucial consideration for the development of new materials and devices for biological applications. Furthermore, as the FIB-SEM method is compatible with a variety of substrate materials and topographies, we expect that this method can be used for more sophisticated *in vivo* studies such as examining the interfaces between osteoblast and titanium implants. We also expect this FIB-SEM method to be compatible with immunolabeling and genetically encoded EM enhancers.[42]

EXPERIMENTAL PROCEDURE

1. Nanostructure Fabrication, Characterization, and Preparation. *Fabrication and Characterization of Quartz Nanopillars, CUIO Structures, Nanobars, and Nanotubes.* Nanostructures (NSs) used in this work were fabricated on a 4 in. quartz wafer using electron-beam lithography (EBL). In brief, the wafer was diced into pieces 2 cm × 2 cm square. After sonication cleaning in acetone and 2-propanol, the pieces were spin-coated with 300 nm of ZEP-520 (ZEON Chemicals), followed by E-Spacer 300Z (Showa Denko). Desired patterns were exposed by EBL (Raith150) and developed in xylene. The mask was then created by sputter deposition of 100 nm Cr and lift-off in acetone. NSs was generated by reactive ion etching with CHF_3 and O_2 chemistry (AMT 8100 etcher, Applied Materials). Before cell culture, the substrate was cleaned in O_2 plasma and immersed in Chromium Etchant 1020 (Transene) to remove Cr masks. SEM (FEI Nova) imaging was performed on 3 nm Cr sputtered substrates to measure the dimensions of different NSs.

Silicon Nanocones. A monolayer polystyrene nanosphere (PS) array, which consists of PSs with an average diameter of 3 μm, was self-assembled on glass-based silicon substrates with the Langmuir–Blodgett method. To control the effective intervals between the formed silicon nanopillars, a reactive ion etching process with oxygen (O_2) as an etching gas was then followed to shrink the PSs (with a final diameter of 1 μm). Silicon nanocones were last formed on glass substrates by introducing chlorine (Cl_2) and hydrogen bromide (HBr) gases to reactive-ion-etch the silicon materials exposed to the plasma.

Quartz Nanopillars with PEDOT:PSS Cover Layer. Fused silica glass substrates were cleaned using a standard soap, acetone, 2-propanol sonication sequence. Poly(3,4-ethylenedioxythiophene) polystyrenesulfonate (PEDOT:PSS) (Heraeus, Clevios PH 1000) solution in water was doped with 5 wt % ethylene glycol (EG), 0.1 wt % dodecyl benzenesulfonic acid (DBSA) as a surfactant, and 1 wt % (3-glycidyloxypropyl)trimethoxysilane (GOPTS) as a cross-linking agent to improve film stability. EG, DBSA, and GOPS were all obtained from Sigma-Aldrich. After spin-coating at 1000 rpm for 2 min the films were baked at 120 °C for 10 min.

Furthermore, the nanopillar substrates were cleaned using an oxygen plasma etch and the standard acetone 2-propanol sequence without ultrasonication to protect the pillars. A similar PEDOT:PSS solution was spin-coated at 3000 rpm for 2 min and subsequently baked for 10 min at 120 °C to create a uniform film covering the pillars.

Nanopores. A 500 μm thick (100) silicon wafer was used for the e-beam writing. The sample was spin-coated with 300 nm of negative electron-sensitive resist Ma-N 2403 (MicroChem Corp.) and then baked at 100 °C for 4 min. The pattern was written using an e-beam lithography system (NanoBeam nB5) at 80 kV and was developed in Ma-D 525 developer (Microchem Corp.). A 50 nm layer of Cr metal was deposited using e-beam evaporation for mask creation. After liftoff, nanopores were created on the silicon wafer, defined by a Cr mask, and etched using an ICP-GSE200 etcher (North Microelectronics). Finally, the Cr mask was removed by concentrated hydrochloric acid.

Silicon Grooves. The samples were manufactured at the Molecular Foundry at Lawrence Berkeley National Laboratory under contract DE-AC02-05CH11231.

FIB-Based Procedure. Quartz substrates were coated with a 200 nm thick layer of platinum. Nanopores (1.5−3 μm diameter, 3−5 μm pitch) were etched by focused ion beam (dual beam Helios 600i, at 30 kV and a current of 40 pA). Afterward, the platinum layer was removed by aqua regia overnight at room temperature.

Sample Preparation for Cell Culture. Quartz substrates were treated with piranha solution with sulfuric acid and hydrogen peroxide (Fisher Scientific), in a 7:1 dilution at room temperature overnight. Samples were washed with distilled water, dried, and placed in 70% ethanol in a sterile hood. Samples were washed with sterile distilled water and allowed to dry. After a 15 min UV light exposure, samples were incubated overnight with 0.01% poly-L-lysine (Sigma Life Science) for primary neurons and HEK cell cultures or with 1 mg/mL fibronectin (Life Technologies) in 0.02% gelatin solution for HL-1 cells. COS-7 cells were directly plated on the substrate after sterilization.

2. Cell Culture and Transfection. *Primary Neurons.* Cortices were extracted from rat embryos at embryonic day 18 and incubated with 0.25% trypsin/EDTA (Corning) in a 33 mm Petri dish for 5 min at 37 °C. The tissue-trypsin/EDTA solution was transferred into a 2 mL plastic tube. The tissue settled at the bottom of the tube, and leftover trypsin/EDTA was removed. Neurobasal media (Gibco) was supplemented with 1% B27 (Gibco), 0.25% glutaMAX (Gibco), and 0.1% gentamycin antibiotic (Gibco). One milliliter of warm media was added, and then the tube was gently swirled by hand. This procedure was repeated five times, and after the last media exchange, the tissue was dissociated until resulting in a cell solution. A total of 80 000 cells were suspended in 3 mL and placed on each substrate. The media was replaced completely 2 h after seeding time. Every second day, half of the media was exchanged with freshly prepared warm (supplemented) Neurobasal media.

HL-1 Cells. Confluent HL-1 cells, cultured in a 33 mm Petri dish, were incubated with 1 mL of 0.25% trypsin/EDTA for 5 min at 37 °C. The cell−trypsin solution was transferred into a 15 mL tube, and 2 mL of Claycomb media (Sigma Life Science) supplemented with 10% fetal bovine serum (Sigma-Aldrich), 100 μg/mL penicillin/streptomycin (Sigma Life Science), 0.1 mM norepinephrine (Sigma-Aldrich), and 2 mM glutaMAX were added. The cell solution was placed in a centrifuge for 3 min with a rotation of 1300 rpm. The cell pellet was resuspended in 1 mL of media, and 50 μL of the resuspension was plated on each substrate in addition to 3 mL of supplemented media.

HEK 293 Cells. HEK 293 expressing channels NaV 1.3 and KIR 2.1 were acquired by Adam Cohen laboratory and maintained in DMEM/F12 (Gibco), 10% FBS (Gibco), 1% penicillin/streptomycin (100 μg/mL, Gibco), Geneticin (500 μg/mL, Gibco), and puromycin (2 μg/mL, Fisher Scientific). At 80% confluency, cells were divided, resuspended, and plated on quartz substrates as for HL-1 cells.

COS-7 and U2OS Cells. Cells were maintained in DMEM supplemented with 10% fetal bovine serum, and at 90% confluency they were divided as for HL-1 cells and plated on the substrates.

CAAX/LifeAct Transfection. U2OS cells were cultured in DMEM medium (HyClone) with 10% fetal bovine serum (Gibco) and 1% penicillin/streptomycin (Invitrogen) at 37 °C in 5% CO_2. Transfection was preformed using electroporation (Amaxa Nucleofector) with the manufacturer's protocol. U2OS cells were transfected with Lifeact-RFP (transformed bacteria acquired from AddGene) and Caax-GFP and plated on a nanostructured surface for at least 16 h before examination.

3. Ultrathin Plastification and RO-T-O Procedure. Substrates with cells were rinsed with 0.1 M sodium cacodylate buffer (Electron Microscopy Sciences) and fixed with 3.2% glutaraldehyde (Sigma-Aldrich) at 4 °C overnight. Specimens were then washed (3 × 5 min) with chilled buffer and quenched with chilled 20 mM glycine solution (20 min). After rinsing (3 × 5 min) with chilled buffer specimens were postfixed with equal volumes of 4% osmium tetroxide and 2%

potassium ferrocyanide (Electron Microscopy Sciences, RO step) (1 h on ice). Samples were then washed with chilled buffer (3 × 5 min), and the solution was replaced with freshly prepared 1% thiocarbohydrazide (Electron Microscopy Sciences, T step) (20 min at room temperature). After rinsing with buffer (2 × 5 min), the samples were incubated with 2% aqueous osmium tetroxide (O step) (30 min at room temperature). Cells were again rinsed (2 × 5 min) with distilled water and then, finally, incubated with syringe-filtered 4% aqueous uranyl acetate (Electron Microscopy Sciences, en bloc step) (overnight 4 °C). Cells were rinsed (3 × 5 min) with chilled distilled water, followed by gradual dehydration in an increasing ethanol series (10%−30%−50%−70%−90%−100%, 5−10 min each on ice). The last exchange with a 100% ethanol solution was performed at room temperature. Epoxy-based resin solution was prepared as previously described,[24] and samples were infiltrated with increasing concentrations of resin in 100% ethanol, using these ratios: 1:3 (3 h), 1:2 (3 h), 1:1 (overnight), 2:1 (3 h), 3:1 (3 h). Infiltration was carried out at room temperature and in a sealed container to prevent evaporation of ethanol. Samples were then infiltrated with 100% resin overnight at room temperature. The excess resin removal was carried out by first draining away most of the resin by mounting the sample vertically for 1 h and, then, rapidly rinsing with 100% ethanol prior to polymerization at 60 °C overnight.

4. Scanning Electron Microscopy Imaging and Focused Ion Beam Sectioning. *Sample Preparation.* Each sample was glued with colloidal silver paste (Ted Pella Inc.) to a standard stub 18 mm pin mount (Ted Pella Inc.). A very thin layer of gold−palladium alloy was sputtered on the sample before imaging.

SEM Imaging. Samples were loaded into the vacuum chamber of a dual-beam Helios Nanolab600i FIB-SEM (FEI). For selecting a region of interest, an (electron) beam with an accelerating voltage of 3−5 kV and current of 21 pA to 1.4 nA was applied. For image acquisition of whole cells (*i.e.*, Figure 1b) a secondary electron detector was used. For cross section imaging, a beam acceleration voltage of 2−10 kV was selected, with the current ranging between 0.17 and 1.4 nA, while using a backscattered electron detector (immersion mode, dynamic focus disabled in cross section, stage bias zero), a dwell time of 100 μs, and 3072 × 2048 pixel store resolution. For the sequential sectioning, the function iSPI was enabled in order to slice and acquire an image of the stack every 38.5 nm with 5 kV voltage, 1.4 nA current, and 1024 × 884 resolution.

FIB Sectioning. Regions of interest were preserved by electron-assisted deposition of a 0.5 μm double platinum layer and ion-assisted deposition of a (nominal) 1 μm thick coating. First, trenches were created with an etching procedure fixing an acceleration voltage of 30 kV and currents in the range 9.1−0.74 nA depending on the effective area to remove. A fine polishing procedure of the resulting cross sections was carried out on the sections, with a voltage of 30 kV and lower currents in the range 0.74 nA to 80 pA so that redeposition phenomena in the cross section are very limited.

Image Analysis and 3D Reconstruction. All images were preprocessed with ImageJ (National Institutes of Health, USA, http://imagej.nih.gov/ij). The images of the sequential cross sections shown in Figure 2 were collected as a stack, analyzed, and processed with an open source tool chain based on Python (Python Software Foundation, USA, http://www.python.org) scripts and tools. The image stack was cropped, filtered, and down-sampled. The isotropic resolution in x, y, and z amounts to 38.5 nm. The reconstructed data are visualized with Blender (Blender Foundation, The Netherlands, http://www.blender.org).

Cleft Distance. The average cleft distance has been calculated by selecting 10 equally distributed points on the part of the plasma membrane that surrounds the nanostructures. For each point, the distance is measured as the shortest distance between the membrane and the material surface. The number of points, the number of nanostructures, and the number of cells that are used to calculate the average number (and the standard deviations of the mean) are listed in Supplementary Table S10. The measurements have been performed with ImageJ.

ASSOCIATED CONTENT

Ⓢ Supporting Information

The Supporting Information is available free of charge on the ACS Publications website at DOI: 10.1021/acsnano.7b03494.

> Movie (AVI)
> Ultrathin plasticization of cells on planar substrates, sectioning procedure, ultrastructure resolution, substrate geometry of nanopillars and nanocones, substrate geometry of nanopores, substrate geometry of CUI, nanobars, nanotubes, and grooves, SEM of cells on a flat surface and diverse nanostructures, cleft between cells and flat, nanopillar, and nanopore surfaces, cleft visualization for cells on complex structures, cleft distance, cleft index, CAAX/ACTIN cotransfection (PDF)

AUTHOR INFORMATION

Corresponding Authors
*E-mail: santorof@stanford.edu.
*E-mail: bcui@stanford.edu.

ORCID ⊙
Yoeri van de Burgt: 0000-0003-3472-0148
Bianxiao Cui: 0000-0002-8044-5629

Present Addresses
□Department of Mechanical Engineering and Institute for Complex Molecular Systems, Eindhoven University of Technology, 5612 AZ, Eindhoven, The Netherlands.
¶Italian Institute of Technology−Center of Advanced Biomaterials and Healthcare, 80125, Naples, Italy.

Notes
The authors declare no competing financial interest.

REFERENCES

(1) Langer, R.; Tirrell, D. A. Designing Materials for Biology and Medicine. *Nature* **2004**, *428*, 487−492.

(2) Anderson, J. M. Biological Responses to Materials. *Annu. Rev. Mater. Res.* **2001**, *31*, 81−110.

(3) Kieswetter, K.; Schwartz, Z.; Dean, D. D.; Boyan, B. D. The Role of Implant Surface Characteristics in the Healing of Bone. *Crit. Rev. Oral Biol. Med.* **1996**, *7*, 329−345.

(4) Rychly, J.; Nebe, B. Interface Biology of Implants. *Cell Adhes. Migr.* **2009**, *3*, 390−394.

(5) Olivares-Navarrete, R.; Hyzy, S. L.; Berg, M. E.; Schneider, J. M.; Hotchkiss, K.; Schwartz, Z.; Boyan, B. D. Osteoblast Lineage Cells Can Discriminate Microscale Topographic Features on Titanium−Aluminum−Vanadium Surfaces. *Ann. Biomed. Eng.* **2014**, *42*, 2551−2561.

(6) Chen, W.; Shao, Y.; Li, X.; Zhao, G.; Fu, J. Nanotopographical Surfaces for Stem Cell Fate Control: Engineering Mechanobiology from the Bottom. *Nano Today* **2014**, *9*, 759−784.

(7) Schneider, G. B.; Perinpanayagam, H.; Clegg, M.; Zaharias, R.; Seabold, D.; Keller, J.; Stanford, C. Implant Surface Roughness Affects Osteoblast Gene Expression. *J. Dent. Res.* **2003**, *82*, 372−376.

(8) Luu, T. U.; Gott, S. C.; Woo, B. W. K.; Rao, M. P.; Liu, W. F. Micro- and Nanopatterned Topographical Cues for Regulating Macrophage Cell Shape and Phenotype. *ACS Appl. Mater. Interfaces* **2015**, *7*, 28665−28672.

(9) Stevens, M. M.; George, J. H. Exploring and Engineering the Cell Surface Interface. *Science* **2005**, *310*, 1135−1138.

(10) Kasemo, B. Biological Surface Science. *Surf. Sci.* **2002**, *500*, 656−677.

(11) Oh, S.; Brammer, K. S.; Li, Y. S. J.; Teng, D.; Engler, A. J.; Chien, S.; Jin, S. Stem Cell Fate Dictated Solely by Altered Nanotube Dimension. *Proc. Natl. Acad. Sci. U. S. A.* **2009**, *106*, 2130−2135.

(12) Toma, K.; Kano, H.; Offenhäusser, A. Label-Free Measurement of Cell−Electrode Cleft Gap Distance with High Spatial Resolution Surface Plasmon Microscopy. *ACS Nano* **2014**, *8*, 12612−12619.

(13) Hanson, L.; Lin, Z. C.; Xie, C.; Cui, Y.; Cui, B. Characterization of the Cell-Nanopillar Interface by Transmission Electron Microscopy. *Nano Lett.* **2012**, *12*, 5815−5820.

(14) Wrobel, G.; Höller, M.; Ingebrandt, S.; Dieluweit, S.; Sommerhage, F.; Bochem, H. P.; Offenhäusser, A. Transmission Electron Microscopy Study of the Cell−sensor Interface. *J. R. Soc., Interface* **2008**, *5*, 213−222.

(15) Kiessling, V.; Tamm, L. K. Measuring Distances in Supported Bilayers by Fluorescence Interference-Contrast Microscopy: Polymer Supports and SNARE Proteins. *Biophys. J.* **2003**, *84*, 408−418.

(16) Lambacher, A.; Fromherz, P. Fluorescence Interference-Contrast Microscopy on Oxidized Silicon Using a Monomolecular Dye Layer. *Appl. Phys. A: Mater. Sci. Process.* **1996**, *63*, 207−216.

(17) Braun, D.; Fromherz, P. Fluorescence Interference-Contrast Microscopy of Cell Adhesion on Oxidized Silicon. *Appl. Phys. A: Mater. Sci. Process.* **1997**, *65*, 341−348.

(18) Ajo-Franklin, C. M.; Ganesan, P. V.; Boxer, S. G. Variable Incidence Angle Fluorescence Interference Contrast Microscopy for Z-Imaging Single Objects. *Biophys. J.* **2005**, *89*, 2759−2769.

(19) Fendyur, A.; Mazurski, N.; Shappir, J.; Spira, M. E. Formation of Essential Ultrastructural Interface between Cultured Hippocampal Cells and Gold Mushroom-Shaped MEA- Toward "IN-CELL" Recordings from Vertebrate Neurons. *Front. Neuroeng.* **2011**, *4*.10.3389/fneng.2011.00014

(20) Hai, A.; Kamber, D.; Malkinson, G.; Erez, H.; Mazurski, N.; Shappir, J.; Spira, M. E. Changing Gears from Chemical Adhesion of Cells to Flat Substrata toward Engulfment of Micro-Protrusions by Active Mechanisms. *J. Neural Eng.* **2009**, *6*, 066009.

(21) Narayan, K.; Subramaniam, S. Focused Ion Beams in Biology. *Nat. Methods* **2015**, *12*, 1021−1031.

(22) Boyde, A.; MacOnnachie, E. Volume Changes during Preparation of Mouse Embryonic Tissue for Scanning Electron Microscopy. *Scanning* **1979**, *2*, 149−163.

(23) Gusnard, D.; Kirschner, R. H. Cell and Organelle Shrinkage during Preparation for Scanning Electron Microscopy: Effects of Fixation, Dehydration and Critical Point Drying. *J. Microsc.* **1977**, *110*, 51−57.

(24) Belu, A.; Schnitker, J.; Bertazzo, S.; Neumann, E.; Mayer, D.; Offenhäusser, A.; Santoro, F. Ultra-Thin Resin Embedding Method for Scanning Electron Microscopy of Individual Cells on High and Low Aspect Ratio 3D Nanostructures. *J. Microsc.* **2016**, *263*, 78−86.

(25) Persson, H.; Købler, C.; Mølhave, K.; Samuelson, L.; Tegenfeldt, J. O.; Oredsson, S.; Prinz, C. N. Fibroblasts Cultured on Nanowires Exhibit Low Motility, Impaired Cell Division, and DNA Damage. *Small* **2013**, *9*, 4006−4016.

(26) Wierzbicki, R.; Købler, C.; Jensen, M. R. B.; Łopacińska, J.; Schmidt, M. S.; Skolimowski, M.; Abeille, F.; Qvortrup, K.; Mølhave, K. Mapping the Complex Morphology of Cell Interactions with Nanowire Substrates Using FIB-SEM. *PLoS One* **2013**, *8*, e53307.

(27) Bittermann, A. G.; Burkhardt, C.; Hall, H. Imaging of Cell-to-Material Interfaces by SEM after in Situ Focused Ion Beam Milling on Flat Surfaces and Complex 3D-Fibrous Structures. *Adv. Eng. Mater.* **2009**, *11*, B182−B188.

(28) Seyock, S.; Maybeck, V.; Offenhäusser, A. How to Image Cell Adhesion on Soft Polymers? *Micron* **2017**, *92*, 39−42.

(29) Collins, V. P.; Arborgh, B.; Brunk, U. A Comparison of the Effects of Three Widely Used Glutaraldehyde Fixatives on Cellular Volume and Structure. *Acta Pathol. Microbiol. Scand., Sect. A* **1977**, *85A*, 157−168.

(30) Jeansson, M.; Haraldsson, B. Morphological and Functional Evidence for an Important Role of the Endothelial Cell Glycocalyx in the Glomerular Barrier. *Am. J. Physiol. - Ren. Physiol.* **2006**, *290*, F111−F116.

(31) Tapia, J. C.; Kasthuri, N.; Hayworth, K. J.; Schalek, R.; Lichtman, J. W.; Smith, S. J.; Buchanan, J. High-Contrast En Bloc Staining of Neuronal Tissue for Field Emission Scanning Electron Microscopy. *Nat. Protoc.* **2012**, *7*, 193−206.

(32) Bushby, A. J.; P'ng, K. M. Y.; Young, R. D.; Pinali, C.; Knupp, C.; Quantock, A. J. Imaging Three-Dimensional Tissue Architectures by Focused Ion Beam Scanning Electron Microscopy. *Nat. Protoc.* **2011**, *6*, 845−858.

(33) Santoro, F.; Neumann, E.; Panaitov, G.; Offenhäusser, A. FIB Section of Cell−electrode Interface: An Approach for Reducing Curtaining Effects. *Microelectron. Eng.* **2014**, *124*, 17−21.

(34) Santoro, F.; Dasgupta, S.; Schnitker, J.; Auth, T.; Neumann, E.; Panaitov, G.; Gompper, G.; Offenhäusser, A. Interfacing Electrogenic Cells with 3D Nanoelectrodes: Position, Shape, and Size Matter. *ACS Nano* **2014**, *8*, 6713−6723.

(35) Moran-Mirabal, J. M.; Torres, A. J.; Samiee, K. T.; Baird, B. A.; Craighead, H. G. Cell Investigation of Nanostructures: Zero-Mode Waveguides for Plasma Membrane Studies with Single Molecule Resolution. *Nanotechnology* **2007**, *18*, 195101.

(36) Richards, C. I.; Luong, K.; Srinivasan, R.; Turner, S. W.; Dougherty, D. A.; Korlach, J.; Lester, H. A. Live-Cell Imaging of Single Receptor Composition Using Zero-Mode Waveguide Nanostructures. *Nano Lett.* **2012**, *12*, 3690−3694.

(37) Atilgan, E.; Wirtz, D.; Sun, S. X. Mechanics and Dynamics of Actin-Driven Thin Membrane Protrusions. *Biophys. J.* **2006**, *90*, 65−76.

(38) Schafer, D. A. Coupling Actin Dynamics and Membrane Dynamics during Endocytosis. *Curr. Opin. Cell Biol.* **2002**, *14*, 76−81.

(39) Hanson, L.; Zhao, W.; Lou, H.-Y.; Lin, Z. C.; Lee, S. W.; Chowdary, P.; Cui, Y.; Cui, B. Vertical Nanopillars for in Situ Probing of Nuclear Mechanics in Adherent Cells. *Nat. Nanotechnol.* **2015**, *10*, 554−562.

(40) Bartlett, W. P.; Banker, G. A. An Electron Microscopic Study of the Development of Axons and Dendrites by Hippocampal Neurons in Culture. I. Cells Which Develop without Intercellular Contacts. *J. Neurosci.* **1984**, *4*, 1944−1953.

(41) Maxwell, W. L. Damage to Myelin and Oligodendrocytes: A Role in Chronic Outcomes Following Traumatic Brain Injury? *Brain Sci.* **2013**, *3*, 1374−1394.

(42) Lam, S. S.; Martell, J. D.; Kamer, K. J.; Deerinck, T. J.; Ellisman, M. H.; Mootha, V. K.; Ting, A. Y. Directed Evolution of APEX2 for Electron Microscopy and Proximity Labeling. *Nat. Methods* **2015**, *12*, 51−54.